Real-Time Nuclear Magnetic Resonance Detection Using Maximum Likelihood Estimation with Single-Shallow-Nitrogen-Vacancy Centers in Quantum Heterodyne Measurements

Akirabha Chanuntranont Daiki Saito Kazuki Otani Tomoki Ota Yuki Ueda Masato Tsugawa Shuntaro Usui Yuto Miyake Tokuyuki Teraji Shinobu Onoda Takahiro Shinada Hiroshi Kawarada Takashi Tanii*

A. Chanuntranont, D. Saito, K. Otani, T. Ota, Y. Ueda, M. Tsugawa, S. Usui, Y. Miyake, Prof. H. Kawarada, Prof. T. Tanii
School of Fundamental Science and Engineering, Waseda University, 3-4-1 Okubo, Shinjuku, Tokyo 169-8555, Japan
Email Address: akirabha@akane.waseda.jp

T. Teraji
National Institute for Materials Science, 1-1 Namiki, Tsukuba, Ibaraki 304-0044, Japan

S. Onoda
National Institutes for Quantum Science and Technology, 1233 Watanuki, Takasaki, Gunma 370-1292, Japan

T. Shinada
Center for Innovative Integrated Electronic Systems, Tohoku University, 468-1 Aramaki-aza-aoba, Aoba, Sendai, Miyagi 980-8572, Japan

Keywords: *quantum NMR, nanopillar, maximum likelihood, NV center, diamond*

Single NV centers in diamond are highly promising quantum NMR sensors. However, their sensing ability is greatly limited by their low SNR. Not only does low SNR make quantum NMR with single NV centers vulnerable to noise, but it also necessitates longer measurement durations so that a sufficient number of observations can be acquired to combat noise. In this paper, we identify two sources of low SNR in qdyne measurements and provide solutions to overcome them. The first source is the high TIR rate at the air-diamond interface, which is solved by fabricating nanopillars on the diamond surface. The second source is the use of FFT as the signal processing method. Instead, we suggest the use of MLE, which requires much fewer data points for peak detection. Our solutions yield a 3.5× improvement in photon count rate and shortens necessary measurement durations by several orders of magnitude.

1 Introduction

Sensors for nanoscale magnetometry are desired across many practices. Applications of such sensors include materials characterization, electronics defect detection, and structural analysis of biomolecules. Over the past decade, many studies have proposed nitrogen vacancy (NV) centers in diamond as promising sensors for quantum magnetometry. Diamond NV centers have a magnetic field sensitivity of $1\,\mathrm{nT}/\sqrt{\mathrm{Hz}}$, six orders of magnitude more sensitive than conventional nuclear magnetic resonance (NMR) sensors, and a magnetic moment sensitivity of 10^{-3} μ_B, among the highest of any known sensor [1]. Furthermore, recent advances in quantum sensing sequences, such as qdyne, have allowed the frequency resolution of diamond NV centers as quantum NMR sensors to scale with total measurement time as $T^{-3/2}$, arbitrarily beyond their T_2 coherence times [2, 3, 4]. Some other advantages of diamond NV centers include their relatively long quantum coherence times at ambient conditions, their susceptibility to optical control and readout, and their bio-compatibility [5, 6]. These properties give diamond NV centers great potential as both high performance quantum sensors in laboratories and for field deployment in commercial settings.

However, despite various demonstrations of their potential, diamond NV centers are still not ready for regular use as quantum sensors. In quantum NMR applications, a few major hurdles that have to be overcome include the poor charge stability of shallow NV centers, the limited number of detectable nuclear species due to insufficient T_2 times, and the poor signal to noise ratio (SNR) of the measurement itself. The first two problems directly affect the ability of the NV center to act as a coherent sensor and to detect various nuclear species. The third problem affects the total measurement duration and the frequency resolution of the obtained NMR spectrum, often necessitating measurement times in the order of hours or days for biologically relevant samples [6, 2, 3, 4]. Overcoming the problem of low SNR would not only shorten the required measurement duration and improve frequency resolution of quantum NMR with NV centers, bringing these sensors closer to commercial readiness, but may also speed up research in the field as a whole. Thus, improving the SNR of diamond NV centers is the focus of this current work.

In this paper, we identify and overcome two sources of low SNR in diamond NV centers for qdyne-based quantum NMR. Particularly, this paper is focused on qdyne measurements with single shallow NV centers, defined as being 5 nm below the diamond surface. The depth of 5 nm was chosen with the goal of single protein structural analysis in mind. NV centers at this depth were shown to have favourable sensing characteristics for protein analysis, such as having a sensing volume that is approximately the size of an individual protein [6]. This paper is organized as follows. In Section 2, we identify the first source of low SNR as the high rate of total internal reflection (TIR) in diamond leading to low photon output. We present the solution to the TIR problem as the fabrication of nanopillars on the diamond surface, resulting in a measured 3.5× increase in photon counts. This result was recently published in [7], but we expand on the discussion here. In Section 3 we identify the second source of low SNR as a sub-optimal choice of signal processing method, namely the fast Fourier transform (FFT). We propose instead the use of maximum likelihood estimation (MLE) and demonstrate significant improvements in peak clarity and orders of magnitude reduction in required measurement duration. In Section 4 we provide a conclusion of our results and directions for future research. Section 5 contains the experimental setup and methods used to obtain our data.

2 Photonic Signal Enhancement with Nanopillars

Most quantum NMR sensing schemes with diamond NV centers are based on optical excitation and readout [8]. Qdyne is a type of an optically based quantum NMR scheme. Optical readout schemes rely on counting single photons emitted from the NV center, thus the photon count rate is a key measure of signal strength [9]. As shown in Figure 1, optical excitation and readout of the NV center state is achieved through the top facet of the diamond. The refractive index of diamond is approximately 2.42 at the air-diamond interface, which corresponds to a narrow critical angle of 24°, beyond which emitted photons are trapped within the diamond due to TIR. The high TIR rate at the air-diamond interface is the physical cause of low SNR in NMR measurements with single diamond NV centers.

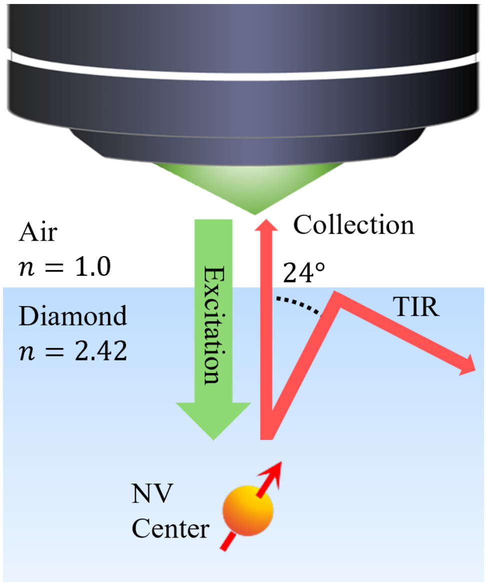

Figure 1: Optical excitation and readout of the NV center state.

Measurements from a single shallow NV center in a diamond sample with a smooth top facet yield a photon count rate of 90 kC/s. Of these counts, approximately 50 kC/s is attributed to background fluorescence. Thus, the NV center contributes only 40 kC/s, which is below the background rate and results in low SNR. In practice, we find that NV center contributions of at least 100 kC/s, or twice the background rate, are required to obtain sufficient SNR for qdyne measurements within tractable time. Various photonic solutions, such as the solid immersion lens [10], the reflecting mirror [11], and the inverted nanocone [12] have been proposed to increase the photon count rate. While these solutions take advantage of diamond's optical properties to increase the photon count rate, they do so without regard for quantum NMR requirements such as NV center depth and charge stability.

A solution that holds promise for quantum NMR applications is the nanopillar. Unlike other pho-

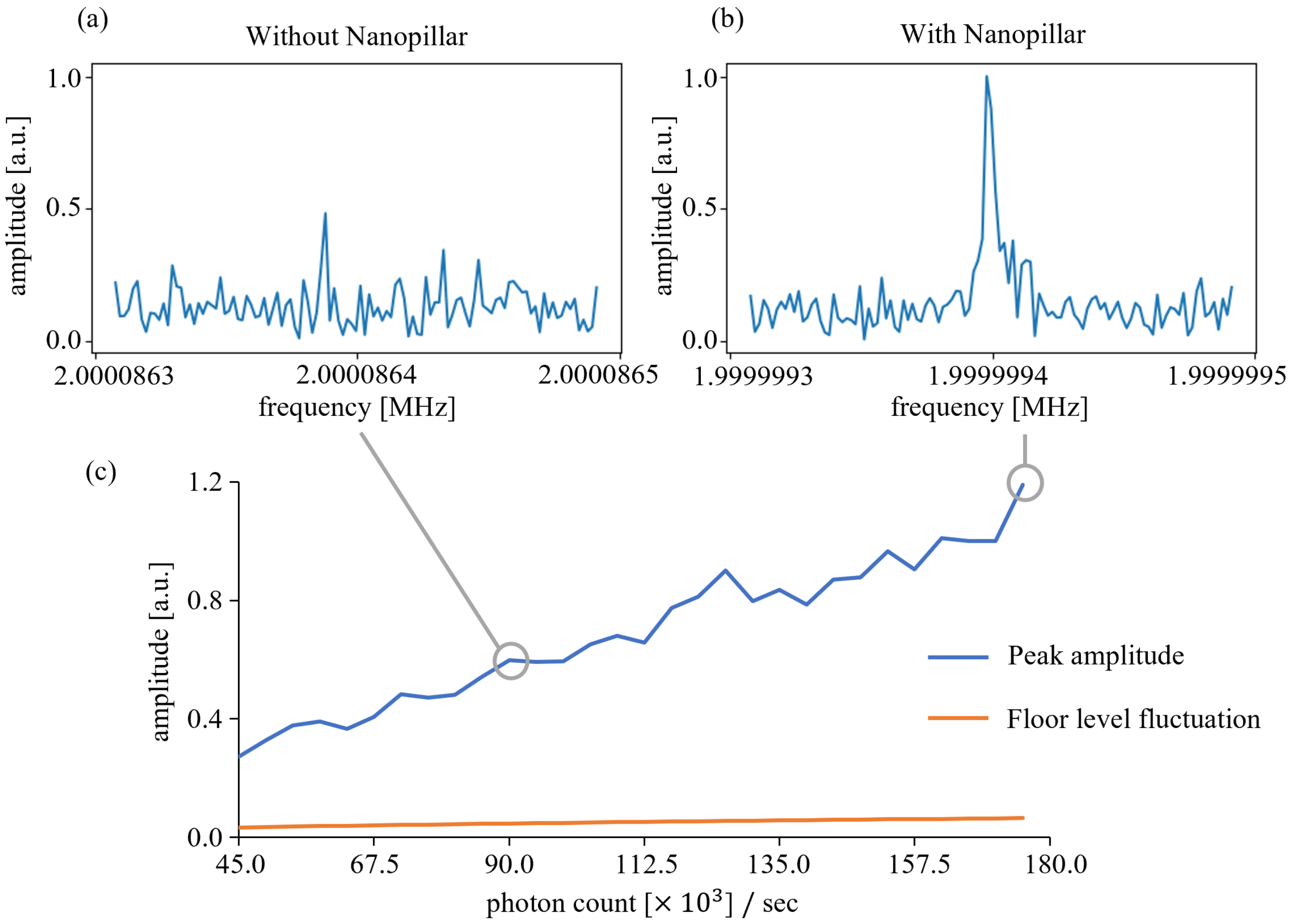

Figure 2: FFT spectrum of observed data for qdyne measurements (a) without a nanopillar and (b) with a nanopillar. (c) Dependence of FFT peak amplitude on photon count rate.

tonic structures, nanopillars do not rely on diamond's optical properties to improve photon count rates. Instead, nanopillars improve photon count rates by exploiting wave-guiding characteristics, coupling photon emission modes to the nanopillar axis so that photons are mainly directed through the top facet of the nanopillar [13]. This mode coupling approach admits greater flexibility in NV center depth, which is a key determinant of sensing properties. While originally optimized for applications with single NV centers at a depth of 20 nm below the top facet [9], we present nanopillars with new dimensions designed for NV centers 5 nm below the top facet for biological sensing applications.

A grid search described in [7] was performed to determine suitable nanopillar dimensions. A nanopillar with a top facet of 93 nm, base of 261 nm and length of 260 nm was fabricated using the method outlined in Section 5. This nanopillar was found to increase the photon count rate to 180 kC/s, while slightly reducing the background counts to 40 kC/s. Thus, the NV center in the nanopillar was found to contribute 140 kC/s, which is both 3.5× greater than the background rate and the rate of the NV center without nanopillars. Hence, an improvement of 3.5× in photon counts was achieved and our condition that the photon counts be at least twice that of the background is satisfied. A detailed analysis of NV center characteristics and nano-NMR results with the nanopillars are available in [7], but it suffices to say that the NV center maintained its NMR sensing capabilities. Notably, the height of this nanopillar is shorter than those used by other groups, whose nanopillars usually exceed 1 µm in length [9]. The focus on short nanopillars is driven by an interest to find the minimal dimensions that satisfy our sensing requirements and not use any more material than is necessary. Although these dimensions may not be globally optimal, they are sufficient for our purpose.

Photon counts alone do not constitute our final signal. In qdyne measurements, the photon counts must be processed to extract frequency data. Usually, this is achieved through the FFT, where resonant frequencies appear as dominant peaks in the FFT spectrum [8, 3, 2, 4]. To see how the improvement in photon counts translates to SNR improvement in the FFT spectrum, the count data obtained from a 60 s 2 MHz coil measurement described in Section 5 was analyzed. The FFT spectra for measurements performed without and with the nanopillar are shown in Figure 2 (a) and (b) respectively. It can be seen that the measurement with the nanopillar yields an FFT peak with twice the amplitude of the mesurement without the nanopillar. Both peaks are correctly situated around the target 2 MHz frequency, with the small descrepancy most likely being owed to slight differences between the clock of the analog signal generator and the data timing generator. The level of noise, measured as the floor level fluctuation, is similar in both spectra. Thus, an SNR improvement of 2× was achieved in the FFT spectrum.

Simulations based on the measured values were performed to examine the relationship between FFT peak amplitude and the photon count rate. The results of these simulations are presented in Figure 2 (c), which shows the average FFT peak amplitude for various photon count rates. The corresponding locations of the experimentally obtained spectra are also indicated by grey circles. It can be seen that the peak amplitude increases linearly with the photon count rate, which is expected from the linear nature of the FFT. Meanwhile, the floor level fluctuation remains approximately constant, if not increasing very slowly with the photon count rate. Thus, increasing the photon count rate is beneficial for quantum NMR measurements and linearly increases the SNR.

3 Statistical Signal Enhancement with Maximum Likelihood Estimation

The most common way to process a qdyne signal is the FFT. The definition of the FFT for time series observations $x_0, ...x_{n-1}$ is shown in Equation 1,

$$X_k = \sum_{m=0}^{n-1} x_m e^{-i2\pi km/n} \tag{1}$$

where $k \in 0, 1, ..., n-1$ and X_k are the relative contributions of each frequency component. The popularity of the FFT is owed largely to its unbiased nature, as it is a pure transform from the time domain to the frequency domain. In this sense, the FFT may be regarded as a naive method of signal processing. Equation 1 does not perform any sort of inference and produces reliable spectra for all time-series data, regardless of their original generating functions.

While the FFT is a reliable and generally applicable tool, its naive nature means it performs poorly at identifying frequencies of interest within noisy signals. The typical method to increase the chance of detection is to acquire more data, which lengthens the duration of the measurement. In biological sensing applications, qdyne measurements usually run in the order of several hours to acquire enough data points for the FFT to successfully identify a peak. Not only is it tedious to wait several hours for raw measurement data, but it is also difficult to control environmental factors over the course of long measurements. Moreover, a lack of quick litmus tests for signal availability often lead to measurements being performed on areas that do not contain particles of interest, which results in wasted time. Thus, a signal processing method with the ability to detect signals with few data points is highly desired.

Statistical inference methods that allow the input of prior knowledge are better solutions for noisy signals with known generating functions. Previously, Bayesian inference via Markov-chain Monte Carlo (MCMC) simulations was proposed as an alternative to the FFT in qdyne measurements [4]. While Bayesian MCMC inference is a powerful statistical inference tool in theory, it is still largely intractable for most real data. For example, we found that running 3,000 steps of Bayesian MCMC inference for qdyne data with 200,000 data points on four Nvidia A10 GPUs required over 100 hours and, at 64-bit precision, occupied over 70 GB of memory. In this case, both the number of MCMC samples and processed data points are still far smaller than those used in actual analysis. For example, a typical qdyne measurement has several billions of data points, for which at least 100,000 steps of MCMC inference are desired. Clearly, Bayesian MCMC inference is still not ready for practical use cases.

Instead, we propose the use of MLE as an excellent alternative for processing qdyne signals. The basic concept of MLE is to measure the likelihood that the data was generated from a certain function and choose function parameters that maximize that likelihood. Both the definition of the likelihood function and the input of known parameters serve as the provision of prior knowledge. To derive the likelihood function, a model of the measurement data must be defined. The raw signal S from the NV center in a qdyne measurement with a single target frequency is given in Equation 2,

$$S = A \sin\left(2\pi\nu\vec{t} + \phi_0\right) \tag{2}$$

where A is the alternating magnetic field strength, ν is the Larmor frequency of the target nuclear spin, $\vec{t}$ is the elapsed probing time and ϕ_0 is the initial phase of the NV center. The qdyne probing protocol relies on the XY8-k sequence, which acts as a filter function $\vec{F}_{\text{xy8k}}$ defined as a square wave in Equation 3,

$$\vec{F}_{\text{xy8k}} = \left\{1_0, 1_1, ..., 1_{\tau/dt_{\text{xy8k}}}, -1_0, -1_1, ..., -1_{\tau/dt_{\text{xy8k}}}\right\}_{\left(\tau 8k/dt_{\text{xy8k}}\right)\left(2\tau/dt_{\text{xy8k}}\right)} \tag{3}$$

where dt_{xy8k} is the discretized time step of the XY8-k sequence, τ is the Rabi period of the NV center, k is the number of repetitions of the XY8 sequence. The magnetic resonance signal B detected by qdyne is masked by this filter function as in Equation 4.

$$B = \int_0^t S \cdot \vec{F}_{\text{xy8k}} \mathrm{dt}_{\text{xy8k}} \tag{4}$$

The signal B determines the quantum state Q of the NV center to be read out. In our measurements, the readout pulse of the XY8-k sequence is a $3\pi/2$ pulse, which corresponds to a cosine readout function. This function is defined in Equation 5,

$$Q = \cos\left(2\pi\gamma_{\text{NV}} B\right) \tag{5}$$

where γ_{NV} is the gyromagnetic ratio of the NV center. As mentioned in Section 2, this readout is detected as photon counts. The photon emissions from an NV center during a qdyne measurement may be modelled as a non-homogenous Poisson process (NHPP). The time-varying arrival rate λ of the detected photons are approximated as in Equation 6,

$$\lambda = \frac{P_{\max} - P_{\min}}{2} Q + \frac{P_{\max} + P_{\min}}{2} + \lambda_{\text{BG}} \tag{6}$$

where λ_{BG} is the arrival rate of background photons and $P_{\max}$, $P_{\min}$ are the average photon counts in states $m_s = 0$ and $m_s = -1$ respectively. The NHPP representation of detected photon counts P is given in Equation 7.

$$P \sim \mathcal{P}\left(\lambda\right) \tag{7}$$

Finally, the log-likelihood function of Equation 7 is shown in Equation 8,

$$\ln p(\vec{Y}|\vec{\theta}) = -\sum_{k=1}^{N} \lambda_k + \sum_{k=1}^{N} Y_k \ln \lambda_k - \sum_{k=1}^{N} \ln\left(Y_k!\right) \tag{8}$$

where $\vec{Y}$ is a vector of observed photon counts, $\vec{\theta}$ is a vector of function parameters, and λ_k is the arrival rate predicted by a model with $\vec{\theta}$ parameters at time k. The log-likelihood is used instead of the direct likelihood function for two reasons. First, the likelihood shrinks exponentially with the number of observations, often beyond the accuracy of 64-bit floating point numbers and resulting in zero likelihood. Second, the log-likelihood is a summation, while the likelihood function is a product, so computing the log-likelihood is more efficient. The MLE model presented in Equation 2 to Equation 8 clearly contains more information about the target signal than the FFT defined in Equation 1. Also, conveniently, despite the arity of the total measurement model, the log-likelihood function is only dependent on the arrival rate λ. Thus, it is possible to reuse the same log-likelihood function for all NHPP photon counting processes while only swapping out the λ model.

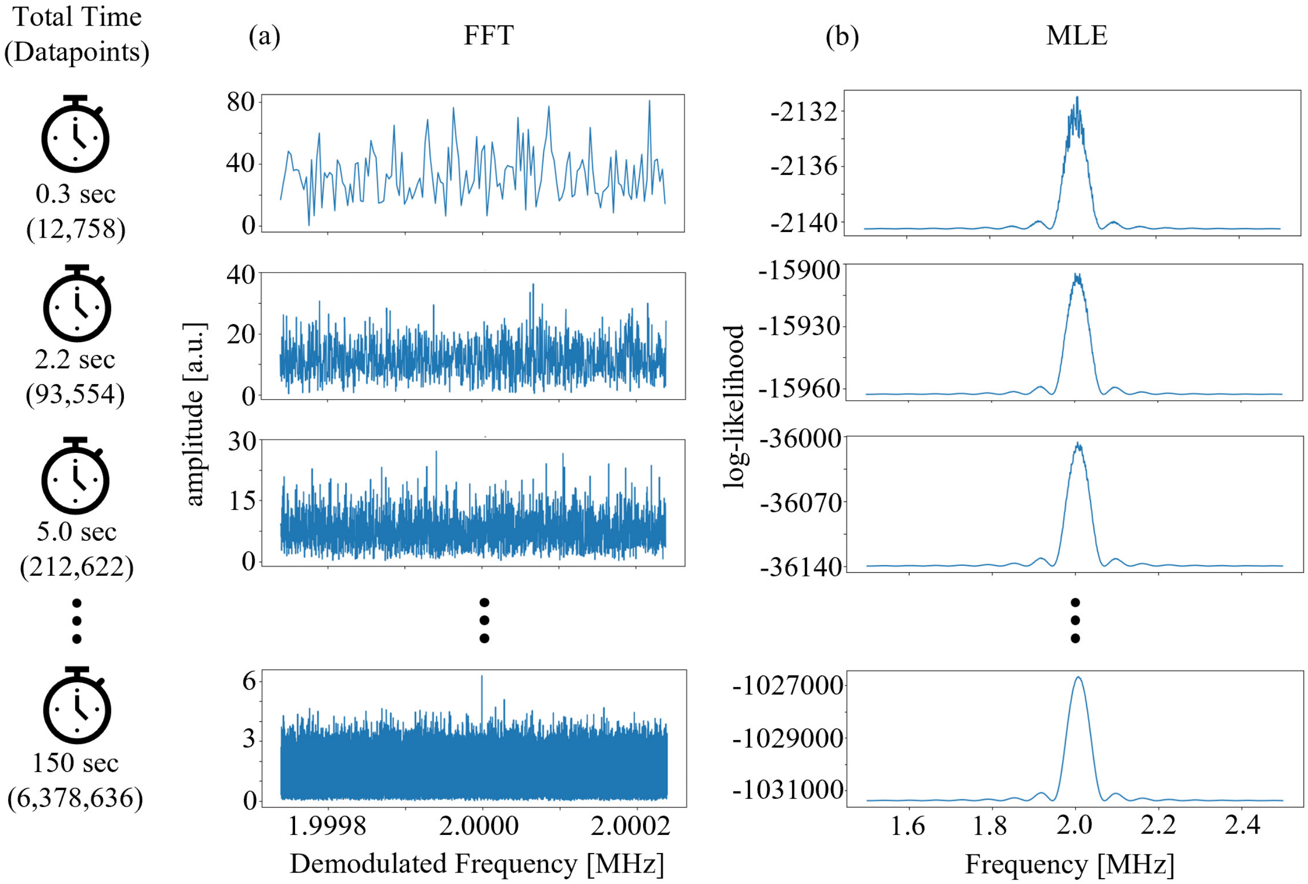

Figure 3: Evolution of the (a) FFT spectrum and (b) MLE likelihood curve for qdyne measurement data at varying elapsed times.

To see whether the prior information improves performance, this model was used to analyze the same coil measurement data from the nanopillar presented in Section 2. The data was truncated at various measurement times in order to see the evolution of the peak shapes as the number of observations is increased. This evolution is shown in Figure 3 (a) and (b) for FFT and MLE analyses respectively. The likelihood curve in the MLE analysis shows the likelihood that the observed data originated from a given frequency. Visually, the likelihood curve is more stable and has a clearer peak than the FFT spectrum across all measurement durations. These characteristics are most likely due to the model's ability to capture noise variances well, leading to stable likelihood curves over time. The likelihood peak is also correctly positioned around 2.0 MHz across all measurement durations, even after only 0.3 s or 12,758 observations. In contrast, the FFT spectrum does not show a clear peak until around 150 s, or approximately 6 million observations. The sensitivity of the FFT lags behind MLE because FFTs perform a pure transform of every data point from the time to frequency domain, while MLE measures the similarity between the observed data and a pre-defined model. Using MLE to process the data requires several orders of magnitude fewer data points than FFT analysis, which translates to significantly shorter measurement durations.

On the other hand, the FFT spectrum is more information dense than the MLE likelihood curve. The FFT spectrum provides the contribution of all constituent frequencies in the signal, while the likelihood curve only searches for one frequency. In principle, it is possible to search for the presence of multiple frequencies using MLE by making a more detailed model, but this comes at the cost of computational efficiency. Similarly, the resolution of the FFT spectrum is significantly higher than that of the MLE likelihood curve. Again, it is possible in principle to improve the resolution of MLE by improving the model, which is an area of active development.

Meanwhile, it should also be noted that the frequency axes of the FFT spectra in Figure 3 are demodulated frequencies, while those of the MLE curves are raw frequencies. Undemodulated FFT spectra from qdyne measurements yield frequencies in the kHz range due to the nature of the heterodyne technique [2]. Thus, the FFT frequencies need to be shifted back into the MHz regime by adding some offset. This technique contributes to the high resolution of FFT, as seen in Figure 3, but the demodulation requires an estimate of the offset, which is often done heuristically and can introduce error. In contrast, MLE analysis accepts frequency inputs as-is due to the use of a complete measurement model. Thus, we can be sure that the likelihood curve corresponds to our frequency axis exactly. Also, as shown in Figure 3, the ability of input frequencies directly into the estimation model allows MLE to search a wider range than FFT.

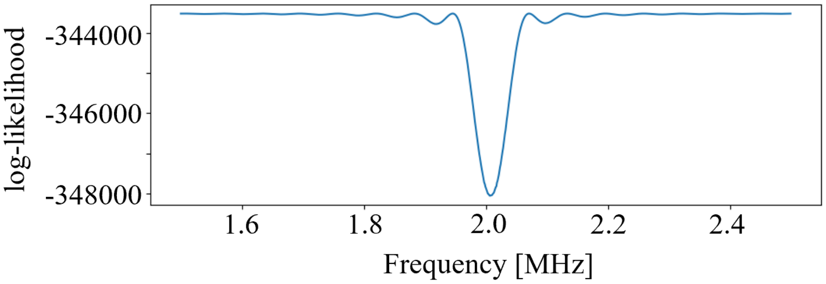

Figure 4: MLE likelihood curve of randomly generated count data.

A concern with MLE is whether it is prone to hallucinations. To explore this question, we used our model to perform MLE on simulated noise data with no underlying signal. A result from this analysis is shown in Figure 4. As can be seen, the likelihood curve in Figure 4 is different from those in Figure 3 (b), with a likelihood dip instead of a peak. The likelihood dip signifies that MLE correctly found no similarity between the data and the proposed model. It is interesting that the likelihood curves in Figure 4 and Figure 3 (b) both show activity in the same range, that is from approximately 1.8 MHz to 2.2 MHz, while the rest of the curve is flat. We believe that the existence of this active region is owed to the frequency filtering properties of the XY8-k sequence, as this active region coincides with the detectable frequencies for the given XY8-k parameters. It makes sense that the likelihood of observations originating from frequencies beyond this filter should be equal, as the model cannot differentiate between those frequencies.

Within this sensitive area, however, peaks will occur when an underlying frequency agrees well with observations and valleys otherwise. From our tests, it appears that the model is robust to hallucinations when the number of observations exceeds 200,000 samples. Nevertheless, more work is needed to develop systematic measures and guards for hallucinations.

4 Conclusion

In this work, two sources of low SNR in qdyne measurements with single shallow NV centers in diamond were identified and overcome. The first source is the high TIR rate of diamond, which is overcome through the fabrication of nanopillars. The nanopillars presented in work increased the photon counts 3.5× and resulted in 2× improvement in FFT SNR. The second source is the choice of signal processing method, for which we suggest the use of MLE. Adopting MLE vastly improves the signal clarity and can potentially reduce necessary measurement durations by orders of magnitude.

The implementation of these two approaches can vastly improve and speed up development of quantum NMR sensing with diamond NV centers. In addition, shortening required measurement durations and improving robustness against noise makes NV centers more attractive for field deployment. However, there are still outstanding issues with both approaches. The variety of nuclear species detectable with NV centers in nanopillars are still limited, likely due to insufficient T_2 times. In MLE, systematic measures and guards for hallucinations must be developed. Until then, we suggest the use of MLE primarily as a litmus test for available particles and frequencies when performing nano-NMR measurements, while using FFT for the final analysis. Solutions to these problems are currently being investigated as part of ongoing research.

5 Experimental Section

Diamond Substrate and NV Centers:
All experiments were performed using a type-Ib high-pressure high-temperature (100) single crystalline diamond substrate with a size of 5 mm×5 mm×1 mm. On the top facet of this substrate, a 20 µm thick 99.95% ^{12}C enriched homoepitaxial diamond film was grown using plasma-assisted chemical vapor deposition as described in [14]. The growth conditions were 140 Torr gas pressure, 1.2 kW microwave power, 120 to 180 W/cm^3 microwave power density, 1% methane concentration, 0% oxygen concentration, 200 sccm total flow rate and 800±10 °C substrate temperature. Single ^{15}N ion implantation was performed in this diamond film at an acceleration energy of 2.5 keV and a fluence of 1.5×10^{11} cm^{-2} as described in [15]. Single NV centers were formed through thermal annealing at 1000 °C in 10% H_2 forming gas. The NV centers were located between 2 nm and 11 nm in depth, with approcimately 50% being located within 4 nm of the surface [15].

Nanopillar Fabrication:
Nanopillars were fabricated on a diamond substrate already containing shallow NV centers following a process described in [7]. The top facet of the diamond substrate was spin coated with PMGI (Microchem, PMGI SF 6S) and ZEP-520A (ZEON, ZEP-520A) at 4000 rpm for 50 s with a slope of 10 s to form a double-layer resist film. The thickness of the PMGI and ZEP-520A layers were measured in a scanning electron microscope (SEM) to be 220 nm and 200 nm respectively. The resist film was baked for 5 min at 225 °C to harden. Electron beam (EB) lithography was performed to pattern regular arrays of nanoholes onto the ZEP-520A layer of the film. The pattern was stabilized in low light through immersion in ZED-N50 for 3 min 30 s followed by a rinse in ZEP for 30 s. Wet etching via immersion in a 2.38% NMD-3 solution for 35 s was performed to transfer the pattern onto the PMGI layer. Ti cylinder masks approximately 130 nm thick were deposited into the nanohole pattern via EB vapor deposition. The diamond was immersed in 20 mL of remover PG and gently perturbed until the double-layer resist film was removed. Inductively coupled plasma (ICP) reactive ion etching with O_2 gas at 30 SCCM and 1 Pa pressure, 700 W ICP power and 250 W bias power was performed to etch the diamond substrate around the

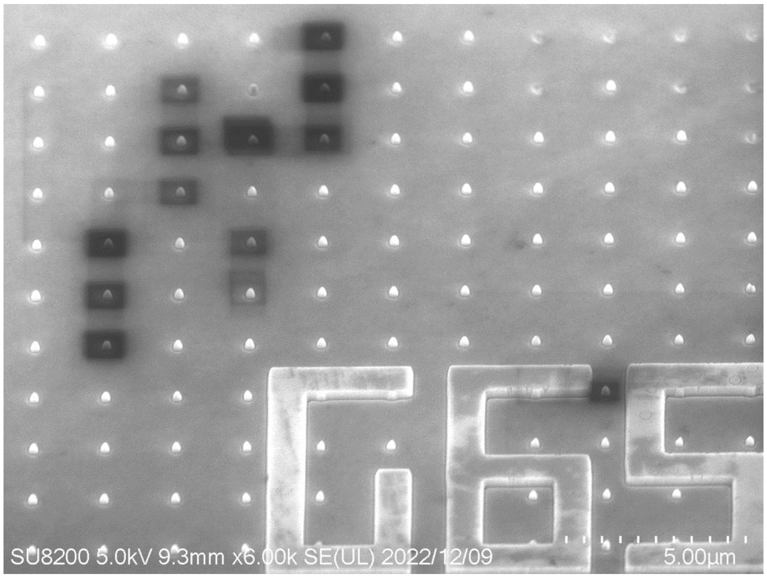

Figure 5: Fabricated nanopillar array.

Ti masks and form nanopillars. The Ti mask was removed through hot mixed acid cleaning ($HNO_3 : H_2SO_4 = 1 : 3$) at 200 °C for 30 min. The diamond surface was terminated with oxygen through O_2 annealing at 465 °C for 8 h to improve the charge stability of the NV centers. A SEM image of the fabricated nanopillar array is shown in Figure 5. It can be seen that this method yields large quantities of highly uniform, evenly spaced nanopillars.

CFM Setup:
A home-built scanning confocal fluorescence microscope (CFM) was used to perform quantum NMR experiments. A schematic of the CFM is shown in Figure 6. Optical control signals were generated by a green 532 nm laser source (Changchun New Industries Optoelectronics Technology, MGL-III-532 nm 300 mW-1%) and pulsed by an acousto-optic modulator (Gooch & Housego, AOMO 3350-120). An air objective lens (Olympus, MPLAPON 50×) was mounted on a piezo stage (PI, NanoCube P-611.3S) for scanning. The diamond was mounted on the sample holder. Microwave (MW) pulses from an analog radio frequency (RF) signal generator (Keysight, E4428C) were pulsed by an RF circuit composed of a phase shifter, two switches and a combiner (Mini-Circuits, ZX10Q-2-25-S+, ZASWA-2-50DR+ and ZX10-2-442-S+) and were amplified by a power amplifier (Mini-Circuits, ZHL-16W-43-S+). A data timing generator (Textronics, DTG5274) controlled RF switching. The MW pulses were supplied to the NV center via a Cu nanowire placed on the diamond surface. A 30 mT static magnetic field was supplied by an Nd magnet. Emissions from the NV center were sent through a long-pass filter (≥650 nm) and detected by a single-photon counting module (Laser Components, COUNT-100C). The photon counting protocol was implemented in a field-programmable gate array (FPGA) board (Digilent, Cora Z7-10) and sent to a desktop computer as binary data. The various components of the CFM were managed using the Qudi software package [16].

Qdyne Measurements:
All qdyne measurements were performed on the same single NV center approximately 5 nm below the diamond surface. The target of the measurements was a 2 MHz alternating magnetic field supplied by a coil wound around the diamond sample. The coil had a loop diameter of 38 mm, wire diameter of 0.40 mm and was hand-wound with 50 turns. A qdyne measurement was first performed on the diamond sample before nanopillar fabrication and again after fabrication. Each measurement was performed for 600 s at ambient conditions.

FFT, MLE and Simulation Implementation:
FFT analysis was performed in Python with the Scipy library [17]. MLE analysis was implemented in Python according to Equation 2 through Equation 8 with the JAX library [18]. This library was cho-

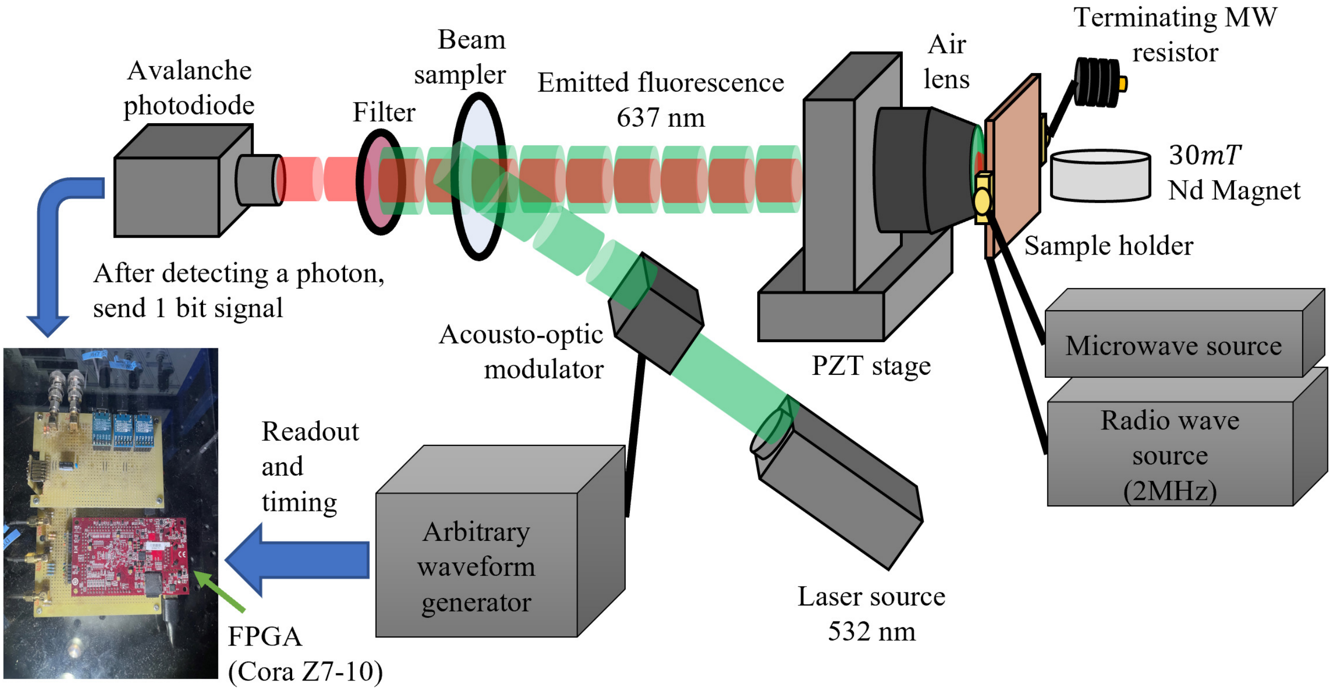

Figure 6: CFM schematic.

sen to take advantage of GPU acceleration. The MLE calculation was sharded across two GPUs (Nvidia 3060) operating in 64-bit precision. Likelihood curves were produced by calculating the log-likelihood of all frequencies from 1.5 MHz to 2.5 MHz with a step of 1 kHz. The measurement model in MLE was also used to simulate qdyne measurement data. These simulations were also sharded across the two GPUs with 64-bit precision.

Acknowledgements

This work was supported by Japan Society for the Promotion of Science (JSPS) KAKENHI (No. JP22H01921, JP18H03766, JP23H00169, 20H02187 and 20H05661), MEXT Q-LEAP (JPMXS0118068379), JST CREST (JPMJCR1773), JST Moonshot R&D (JPMJMS2062), MIC R&D for construction of a global quantum cryptography network (JPMI00316), Advanced Research Infrastructure for Materials and Nanotechnology in Japan (ARIM) and Design & Engineering by Joint Inverse Innovation for Materials Architecture (DEJI^{2}MA) of the Ministry of Education, Culture, Sports, Science and Technology (MEXT).

Conflict of Interest

The authors bear no conflict of interest in this work.

References

[1] M. Chen, C. Meng, Q. Zhang, C.-K. Duan, F. Shi, J. Du, *National Science Review* **2017**, *5*.

[2] S. Schmitt, T. Gefen, F. M. Stürner, T. Unden, G. Wolff, C. Müller, J. Scheuer, B. Naydenov, M. Markham, S. Pezzagna, J. Meijer, I. Schwarz, M. Plenio, A. Retzker, L. P. McGuinness, F. Jelezko, *Science* **2017**, *356*, 6340 832.

[3] J. M. Boss, K. S. Cujia, J. Zopes, C. L. Degen, *Science* **2017**, *356*, 6340 837.

[4] I. Schwartz, J. Rosskopf, S. Schmitt, BenediktTratzmiller, QiongChen, L. P. McGuinness, F. Jelezko, M. B. Plenio, *Scientific Reports* **2019**, *9*, 6938.

[5] A. Gruber, A. Dräbenstedt, C. Tietz, F. Ludovic, J. Wrachtrup, C. Borczyskowski, *Science* **1997**, *276* 2012.

[6] I. Lovchinsky, A. O. Sushkov, E. Urbach, N. P. de Leon, S. Choi, K. D. Greve, R. Evans, R. Gertner, E. Bersin, C. Müller, L. McGuinness, F. Jelezko, R. L. Walsworth, H. Park, M. D. Lukin, *Science* **2016**, *351*, 6275 836.

[7] A. Chanuntranont, K. Otani, D. Saito, Y. Ueda, M. Tsugawa, S. Usui, Y. Miyake, T. Teraji, S. Onoda, T. Shinada, H. Kawarada, T. Tanii, *Applied Physics Express* **2023**, *16*, 8 082006.

[8] E. Abe, K. Sasaki, *Journal of Applied Physics* **2018**, *123*, 161101.

[9] B. J. M. Hausmann, T. M. Babinec, J. T. Choy, J. S. Hodges, S. Hong, I. Bulu, A. Yacoby, M. D. Lukin, M. Loncar, *New Journal of Physics* **2011**, *13*, 045004.

[10] J. P. Hadden, J. P. Harrison, A. C. Stanley-Clarke, L. Marseglia, Y.-L. D. Ho, B. R. Patton, J. L. O'Brien, J. G. Rarity, *Applied physics letters* **2010**, *97*, 24 241901.

[11] S. Furuyama, K. Tahara, T. Iwasaki, M. Shimizu, J. Yaita, M. Kondo, T. Kodera, M. Hatano, *Applied Physics Letters* **2015**, *107*, 16 163102.

[12] C. G. Torun, P.-I. Schneider, M. Hammerschmidt, S. Burger, J. H. D. Munns, T. Schröder, *Applied Physics Letters* **2021**, *118*, 23 234002.

[13] B. J. Hausmann, M. Khan, Y. Zhang, T. M. Babinec, K. Martinick, M. McCutcheon, P. R. Hemmer, M. Lončar, *Diamond and Related Materials* **2010**, *19*, 5 621, proceedings of Diamond 2009, The 20th European Conference on Diamond, Diamond-Like Materials, Carbon Nanotubes and Nitrides, Part 1.

[14] T. Teraji, T. Yamamoto, K. Watanabe, Y. Koide, J. Isoya, S. Onoda, T. Ohshima, L. J. Rogers, F. Jelezko, P. Neumann, J. Wrachtrup, S. Koizumi, *physica status solidi (a)* **2015**, *212*, 11 2365.

[15] R. Fukuda, P. Balasubramanian, I. Higashimata, G. Koike, T. Okada, R. Kagami, T. Teraji, S. Onoda, M. Haruyama, K. Yamada, M. Inaba, H. Yamano, F. M. Stürner, S. Schmitt, L. P. McGuinness, F. Jelezko, T. Ohshima, T. Shinada, H. Kawarada, W. Kada, O. Hanaizumi, T. Tanii, J. Isoya, *New Journal of Physics* **2018**, *20*, 8 083029.

[16] J. M. Binder, A. Stark, N. Tomek, J. Scheuer, F. Frank, K. D. Jahnke, C. Müller, S. Schmitt, M. H. Metsch, T. Unden, T. Gehring, A. Huck, U. L. Andersen, L. J. Rogers, F. Jelezko, *SoftwareX* **2017**, *6* 85.

[17] P. Virtanen, R. Gommers, T. E. Oliphant, M. Haberland, T. Reddy, D. Cournapeau, E. Burovski, P. Peterson, W. Weckesser, J. Bright, S. J. van der Walt, M. Brett, J. Wilson, K. J. Millman, N. Mayorov, A. R. J. Nelson, E. Jones, R. Kern, E. Larson, C. J. Carey, İ. Polat, Y. Feng, E. W. Moore, J. VanderPlas, D. Laxalde, J. Perktold, R. Cimrman, I. Henriksen, E. A. Quintero, C. R. Harris, A. M. Archibald, A. H. Ribeiro, F. Pedregosa, P. van Mulbregt, SciPy 1.0 Contributors, *Nature Methods* **2020**, *17* 261.

[18] J. Bradbury, R. Frostig, P. Hawkins, M. J. Johnson, C. Leary, D. Maclaurin, G. Necula, A. Paszke, J. VanderPlas, S. Wanderman-Milne, Q. Zhang, JAX: composable transformations of Python+NumPy programs, **2018**, URL `http://github.com/google/jax`.

Table of Contents

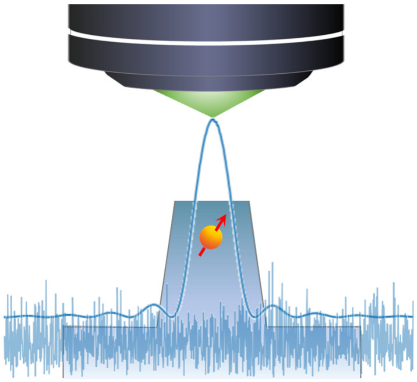

Single NV centers in diamond are highly promising quantum NMR sensors, but are greatly limited by their low SNR. Two methods to increase their SNR are proposed. The first method is fabricating nanopillars, which yields a 3.5× improvement in photon count rate. The second method is using MLE, which shortens necessary measurement durations by several orders of magnitude.